Influencing Flow Patterns and Bed Morphology in Open Channels and Rivers by Means of an Air-Bubble Screen

Violaine Dugué, Ph.D.[1]; Koen Blanckaert, Ph.D.[2]; Qiuwen Chen[3]; and Anton J. Schleiss[4]

Abstract: The ability of a bubble screen to redistribute the flow field and bed morphology in shallow rivers and open channels has been investigated in laboratory experiments. Rising air bubbles generated by a pressurized porous tube situated on the bed induced secondary flow perpendicular to the porous tube. The secondary flow redistributed the longitudinal velocity, which caused also morphological redistribution under mobile-bed conditions. The strength and size of the bubble-induced secondary flow were independent of the base flow velocity and increased with water depth. The size of the secondary flow cell ranged from 3× (immobile bed) to 7× (mobile bed) the water depth. Similar sizes of bubble-induced secondary flow cells have been reported in literature for water depths ranging from 0.1 to 5 m, indicating that the laboratory experiments are relevant for natural rivers and open channels. A mutually strengthening interplay occurred between the bubble screen, the bubble-induced secondary flow, and the morphology. The bubble-induced secondary flow considerably increased the rising velocity of the air bubbles, which on its turn strengthened the secondary flow. The morphological redistribution increased the flow depth in the region covered by the secondary flow cell, which on its turn increased the size and strength of the secondary flow cell, and its effect on the morphological redistribution. This coupled hydrodynamic-morphologic behavior explains the larger size and strength of the secondary flow over a mobile bed than over a flat immobile bed. The results demonstrate the potential of the bubble screen as a technique to modify the morphology in a variety of applications in shallow rivers and open channels. **DOI: 10.1061/(ASCE)HY.1943-7900.0000946.** *© 2014 American Society of Civil Engineers.*

Author keywords: Bubble screen; Channel; Hydrodynamics; Morphology; River; Secondary flow.

Introduction

Line plumes, curtains, or screens of air bubbles are encountered in the management and engineering of water resources at different spatial scales. They have been widely used for promoting destratification and aeration in lakes (Schladow 1992; Wüest et al. 1992), reservoirs (Sahoo and Luketina 2006), or wastewater-treatment systems (DeMoyer et al. 2003; Bombardelli et al. 2007) with the aim to improve water quality or to prevent growth of algae. Bubble curtains have been installed perpendicular to the base flow in harbor entrances to prevent saltwater intrusion (Nakai and Arita 2002), as fish barriers to stop the spread of invasive species in estuaries (Sager et al. 1987; Welton et al. 2002), or as an artificial aeration in ice-covered rivers (Neto et al. 2007).

Knowledge of the surrounding flow induced by the air bubbles is important for most applications and has been largely studied

(Table 1). According to Fanneløp et al. (1991), two regions of recirculating flow, called primary cells, are found on both sides of a line-source air-bubble screen in still-water conditions. Their size varies from 2.5 to 7× the water depth independent of depth and air discharge, except at very low air discharge (Wen and Torrest 1987; Riess and Fanneløp 1998). The cores of the two cells, also called rotor cores, are located close to the bubble screen, independently of the air discharge.

Only few studies have examined the effect of the channel geometrical parameters b (distance between the air-line source and the opposite bank), L (length of the air-line source), and H (cross-sectional averaged water depth; Fig. 1) on the characteristics of the bubble-induced secondary flow. Riess and Fanneløp (1998) determined that the length-to-depth ratio L/H is a characteristic parameter for the secondary flow in still-water conditions. If L/H is lower or higher than unity, the cell is rather small. The largest cell was found with a L/H ratio of unity. Experiments with different air discharges and water depths, but with the same L/H ratio, showed similar behavior. The effect of boundary conditions in still-water conditions was also investigated by Neto et al. (2008) on a circular bubble plume, generated by a single-source nozzle. A large recirculating cell was generated in both square and rectangular tanks but strong three-dimensional (3D) effects appeared in the latter due to the asymmetric configuration of the tank. In their confined setup, two secondary flows were observed in the vertical plane.

Nakai and Arita (2002) studied the application of an air curtain perpendicular to the base flow in rivers in order to prevent saline wedge intrusion. They observed that the characteristics of the bubble-induced flow patterns depend on the relative importance of the buoyancy of the air curtain A and the inertial force of the water flow R

$$A = (q_a g)^{1/3} \tag{1}$$

$$R = q_f/H \tag{2}$$

---

[1]Laboratory of Hydraulic Constructions (LCH), Ecole Polytechnique Fédérale de Lausanne (EPFL), Station 18, CH-1015 Lausanne, Switzerland (corresponding author). E-mail: violaine.dugue@gmail.com

[2]Research Center for Eco-Environmental Sciences, State Key Laboratory of Urban and Regional Ecology, Chinese Academy of Sciences, Beijing 100864, China; and Laboratory of Hydraulic Constructions (LCH), Ecole Polytechnique Fédérale de Lausanne (EPFL), Station 18, CH-1015 Lausanne, Switzerland.

[3]Professor, Research Center for Eco-Environmental Sciences, State Key Laboratory of Urban and Regional Ecology, Chinese Academy of Sciences, Beijing 100864, China.

[4]Professor, Laboratory of Hydraulic Constructions (LCH), Ecole Polytechnique Fédérale de Lausanne (EPFL), Station 18, CH-1015 Lausanne, Switzerland.

Table 1. Line-Source Bubble Plume Experiments Listed in Chronological Order

Reference	B (m)	L (m)	H (m)	L/H (m)	b/H (dimensionless)	Air source	q_a (dm³ s⁻¹ m⁻¹)	Flow conditions
Wen and Torrest (1987)	2.4	0.3	0.6, 1.2	0.25, 0.5	4, 2	Perforated pipe and porous tube	0.68–11.52	Still water
Fanneløp et al. (1991)	20	1	1	1	20	Steel perforated pipe	0.87–4.8	Still water
Riess and Fanneløp (1998), setup 1	20	1	0.5, 1	1, 2	20, 40	Steel perforated pipe	1–4.5	Still water
Riess and Fanneløp (1998), setup 2	20	0.5	0.5, 1	0.5, 1	20, 40	Steel perforated pipe	1–4.5	Still water
Riess and Fanneløp (1998), setup 3	20	0.25	0.5, 1	0.25, 0.5	20, 40	Steel perforated pipe	0–0.417	Still water
Nakai and Arita (2002)	10.4	0.05	0.2	0.25	52	Perforated circular cylinder	0.028–0.042	Perpendicular flow
Blanckaert et al. (2008)	1.1	6.5	0.159	40.88	6.92	Porous tube	0.059–0.277	Longitudinal flow
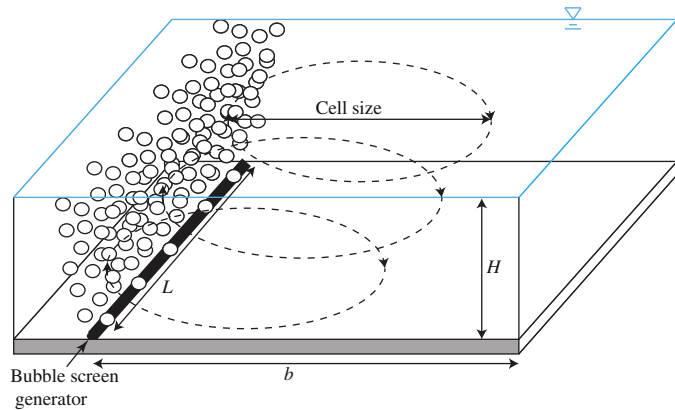
Fig. 1. (Color) Definition sketch of relevant parameters; b is the transverse distance between the air line-source and the opposite bank, L the length of the air line-source, H the water depth, and q_a the air discharge per unit length of air line-source

where g = gravitational acceleration; q_a = air discharge per unit of air-line source length; and q_f = water discharge per unit width. If $A \gg R$, convection by the base flow is weak and the bubble-induced vertical jet spreads to both sides of the air curtain near the water surface. If $A \ll R$, convection by the base flow is so strong that the bubble-induced vertical jet only spreads to the downstream side of the air curtain.

Air bubbles could have interesting engineering applications in shallow rivers. Local scour, for example near bridge piers and abutments or in channel bends, is often caused by vertical velocities impinging on the channel bed. The rising air-bubbles have the potential to counteract these downwards vertical velocities. Moreover, secondary flow cells, such as those induced by the air bubbles, are efficient in redistributing the patterns of velocity and boundary shear stress (Blanckaert and Graf 2004). The advantages of this technique would be the reversibility and possible nonpermanent use of the bubble screen in contrast to most existing engineering techniques.

However, results from the previous investigations on bubble screens cannot straightforwardly be extended to their application parallel to the base flow direction in shallow rivers. The characteristics of the bubble-induced flow patterns can be expected to depend on the flow shallowness and on the velocity of the base flow. Moreover, in relatively narrow rivers they can be expected to be influenced by the riverbanks.

The potential of air-bubble screens in shallow open channels and rivers was first investigated by Blanckaert et al. (2008),

who reported one experiment in a straight open-channel flume and one experiment in a curved shallow open-channel flume under similar flow conditions. Both experiments were performed on a fixed horizontal bed and investigated only hydrodynamic aspects. These experiments have shown that a longitudinal bubble screen, parallel to the flow direction, can generate a bubble-induced secondary flow perpendicular to the bubble screen with a size of about 4× the water depth. This size is in agreement with the previously mentioned studies under still-water conditions (Wen and Torrest 1987; Fanneløp et al. 1991). Blanckaert et al. (2008) have shown that the bubble-induced secondary flow causes redistribution of the longitudinal velocity and of the boundary shear stress, which suggests that the bubble screen would also lead to morphological redistribution in configurations with mobile riverbed.

Dugué et al. (2013) have performed experiments under one hydraulic condition in the same curved laboratory flume as Blanckaert et al. (2008). Instead of fixing a horizontal bed, Dugué et al. (2013) performed experiments under clear-water scour conditions. Under clear-water scour conditions, no sediment is fed to the flume and the critical shear stress necessary for transporting sediment is not exceeded in the straight inflow reach of the flume. Due to curvature-induced flow, the critical shear stress is initially exceeded in parts of the curved reach, leading to sediment transport and the development of a bar-pool bed topography that is typical for open-channel bends. Because no sediment is fed to the flume, sediment transport ultimately vanishes and a stable topography is formed. Dugué et al. (2013) have shown that the bubble screen considerably modifies the ultimate bed topography under clear-water scour conditions. These results suggest that bubble screens could represent a useful tool for influencing morphodynamics in shallow rivers. Clear-water scour conditions are, however, not representative for morphologically important events occurring in natural rivers, which are characterized by live-bed sediment transport.

The objective of the present paper is to extend the previous investigations by Blanckaert et al. (2008) and Dugué et al. (2013). The parameter space will be extended by investigating various conditions of shallowness and base flow velocity, and experiments will be performed with live-bed sediment transport. The main objectives of the paper are to investigate the following:
- The effects of flow shallowness under still-water and flowing-water conditions,
- The effects of the base flow velocity,
- The effects of live-bed sediment transport, and
- The interplay between the air-bubble screen, the bubble-induced secondary flow, the patterns of longitudinal flow, and the morphology.

The research reported in this paper is limited to configurations with fixed sidewalls.

Experiments and Measurements

Experimental Setup

Laboratory experiments were performed in a 9-m long straight open channel at Ecole Polytechnique Fédérale de Lausanne (EPFL). The flume had a rectangular cross section of constant width $B = 1.3$ m with smooth PVC vertical walls [Fig. 2(a)]. A movable weir enabled controlling the water level in the flume. The bed was horizontal and covered with a quasi-uniform quartz sand with a mean diameter $d_m = 0.002$ m.

An orthogonal Cartesian reference system (x, y, z) was adopted where the longitudinal x-axis coincides with the centerline of the flume, starts at the upstream extremity of the bubble screen, and points in the downstream direction; the transversal y-axis points in the left-direction; and the vertical z-axis upwards. This representation has been adopted in order to facilitate comparison with preliminary experiments performed in the same channel (Blanckaert et al. 2008; Blanckaert 2010).

The bubble screen was generated by means of a porous tube of inner diameter 0.01 m (high-pressure tube of porous rubber, Multivis Waterbehandeling B. V.), installed on the bed at 0.2 m from the left bank parallel to the longitudinal direction of the flume. It was composed of fine holes located on both sides of the diameter, approximately 3-mm apart in longitudinal direction. Air from the

laboratory high-pressure network was supplied at both ends of the porous tube to guarantee a quasi-constant pressure along its entire length. The air discharge was measured in the supply line with a rotameter and kept constant for all experiments, with an air discharge per unit meter of porous tube length of about $0.24 \text{ dm}^3 \text{ s}^{-1} \text{ m}^{-1}$. Based on analysis of photography, the diameter of the bubbles was estimated to vary between 0.002 and 0.015 m, with an average diameter of about 0.005 m. The porous tube was installed from 4-m downstream of the flume entrance onto the flume exit and was ballasted on its whole length with a chain to avoid its movement.

Velocity Measurements

Nonintrusive velocity measurements were performed with an acoustic doppler velocity profiler (ADVP), developed at EPFL (Lemmin and Rolland 1997; Hurther and Lemmin 1998; Blanckaert and Lemmin 2006). The ADVP consists of a central emitter surrounded by four receivers, placed in a housing that touches the water surface. It measures the quasi-instantaneous velocity vector simultaneously along the entire water column [Fig. 2(b)]. From these measurements, the time-averaged velocities $\mathbf{v}$ in the three directions, i.e., (1) $\mathbf{v_x}$, (2) $\mathbf{v_y}$, and (3) $\mathbf{v_z}$, are derived. The housing induces flow perturbations near the water surface, which can be bridged by means of extrapolations
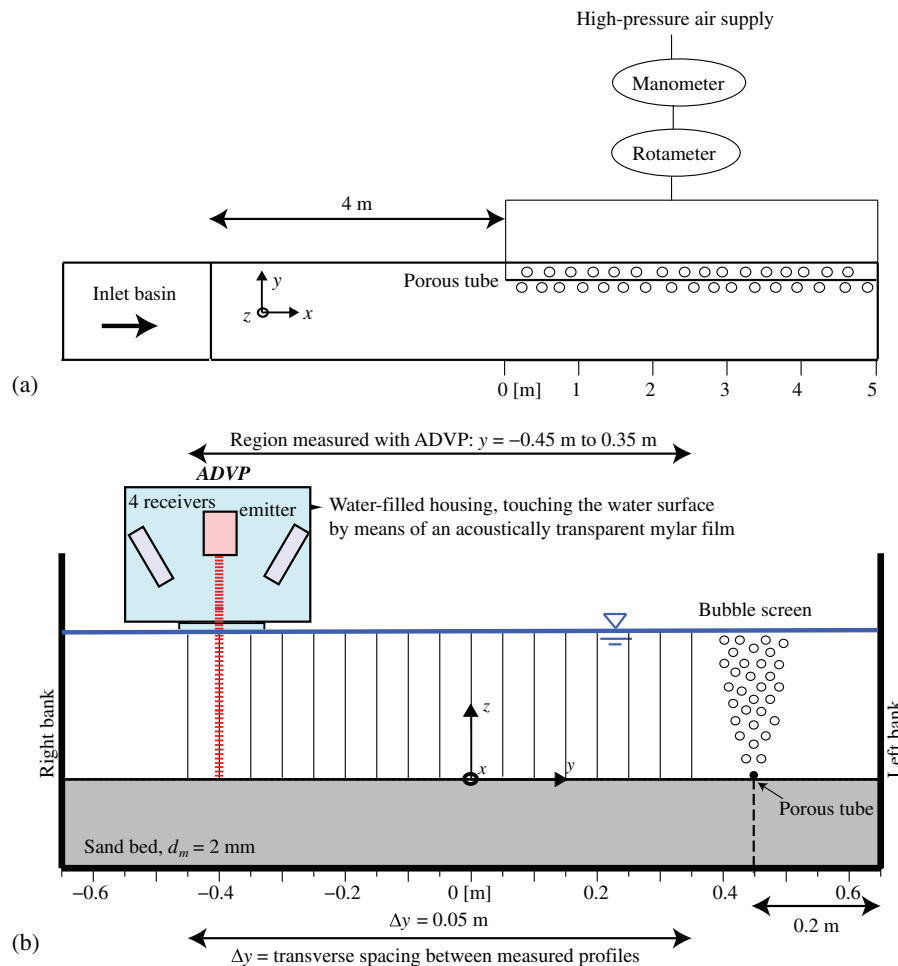
Fig. 2. (Color) (a) Plan view of the channel with the porous tube installed on the bed; (b) scheme of the velocity measurements performed in a cross-section with the acoustic Doppler velocity profiler

(Blanckaert 2010). The uncertainty in the longitudinal velocity component $\mathbf{v_x}$ is estimated at about 4% and in the secondary flow velocities ($\mathbf{v_y}$, $\mathbf{v_z}$) at about 10% (Blanckaert 2010).

Wandering (periodic oscillations) of bubble plumes with oscillation frequencies from 0.002–0.003 Hz (García and García 2006) to 0.1–0.2 Hz (Rensen and Roig 2001) have been observed in previous investigations. No wandering of the bubble screen was observed in the research reported in this paper. Therefore, a total measuring duration of 100 s was adopted, which was largely enough to obtain reliable estimates of time-averaged flow quantities. Velocity measurements were performed with a frequency of 31.25 Hz, which provided accurate statistics on the mean flow and turbulence characteristics (Blanckaert and Lemmin 2006).

Experimental Conditions

The experiments were performed under three different conditions, as follows: (1) still water, (2) flow on an immobile flat sand bed, and (3) flow on a mobile sand bed with active sediment transport. Table 2 shows the experimental parameters for all investigated conditions.

The ADVP velocimeter requires a water depth larger than 0.1 m for high-quality measurements. In order to obtain results that are representative for shallow natural rivers, the experiments were designed to avoid interaction between the bubble-induced secondary flow and the opposite vertical sidewall. Because the Blanckaert et al. (2008) experiment in the same straight flume, listed as SF_16_4 (Table 2), indicated that the transverse size of the bubble-induced secondary flow cell is about $4H$, this defined the maximum allowable water depth in the experiments as $(1.3 - 0.2 \text{ m})/4 = 0.275$ m. Based on these constraints, experiments were performed for water depths in the range between $H = 0.11$ and 0.21 m.

In the still-water experiments, the flume was filled with water and closed at both ends. In the straight flow experiments, the flow depth was controlled with a flap gate at the end of the channel. The base flow longitudinal velocities were chosen in order to avoid bed-load sediment transport. Velocity profiles were measured in the cross section at $x = 3$-m downstream from the origin of the porous tube, on a grid with a transverse spacing of 0.05 m in the range $y = -0.45$ to 0.45 m [Fig. 2(b)]. However, the presence

of bubbles caused disturbances in the acoustic signal, leading to erroneous measurements in the region $y > 0.35$ m. Erroneous measurements have been eliminated and are not included in the remainder of the paper. Water surface and bed elevations in the investigated cross section were measured by means of a point gauge.

In the mobile-bed experiment, a constant sediment feeding of $q_s = 0.025$ kg m^{-1} s^{-1} was supplied at the flume entrance and a velocity was chosen that is sufficient to transport the sediment as bed load. Sediment settled down in a settling basin located downstream of the straight reach. The bubble screen was installed at the same location than in the previous experiments and the LB_B experiment was performed until morphological equilibrium was reached. For this experiment, ADVP measurements were performed in six cross sections at (1) $x = 2$-m, (2) $x = 2.5$-m, (3) $x = 3.0$-m, (4) $x = 3.5$-m, (5) $x = 4.0$-m, and (6) $x = 4.5$-m downstream from the origin of the porous tube, on the same cross-sectional grid as in the immobile-bed experiments. The bed elevation was measured by means of a laser distometer on a grid with a longitudinal spacing of 0.1 m between $x = 1$ and 5 m, and a transverse spacing of 0.05 m. Water surface elevations were measured with a manual point gauge.

Method of Analysis

In order to facilitate comparisons, the bubble-induced secondary flow will be visualized by means of the streamfunction ψ (Batchelor 1967)

$$\psi = \frac{1}{2}(\psi_y + \psi_z) \tag{3}$$

$$\psi_y = -\int_{z_b}^{z} \mathbf{v_y} dz \tag{4}$$

$$\psi_z = \int_{y_{min}}^{y_{max}} \mathbf{v_z} dy + C \tag{5}$$

in which z_b = bed elevation; the integration constant C is chosen such that the cross-sectional averaged values of ψ_y and ψ_z are equal; and y_{max} and y_{min} represent the transverse limits of the measuring grid in the considered cross section. Similar to

Table 2. Experimental Conditions

Label[a]	Q (l s^{-1})	H (m)	$\mathbf{U}$ (m s^{-1})	F (dimensionless)	B/H (dimensionless)	b/H (dimensionless)
SW_11	—	0.11	—	—	12.1	10.0
SW_16	—	0.16	—	—	8.3	6.9
SW_21	—	0.21	—	—	6.1	5.2
SF_11_1	13	0.11	0.09	0.09	12.1	10.0
SF_11_2	26	0.11	0.19	0.18	12.1	10.0
SF_11_3	39	0.11	0.28	0.27	12.1	10.0
SF_16_1	19.5	0.16	0.09	0.08	8.2	6.9
SF_16_2	39	0.16	0.19	0.15	8.2	6.9
SF_16_3	58.5	0.16	0.28	0.23	8.2	6.9
SF_16_4[b]	89	0.16	0.43	0.35	8.2	6.9
SF_21_1	26	0.21	0.10	0.07	6.3	5.2
SF_21_2	52	0.21	0.19	0.13	6.3	5.2
SF_21_3	78	0.21	0.29	0.20	6.3	5.2
LB_B	75	0.12	0.47	0.42	10.5	9.2

Note: F = Froude number; H = cross-sectional averaged water depth; Q water discharge; and $\mathbf{U} = Q/(BH)$ = cross-sectional averaged velocity.
[a]The first part of the experiment label refers to live bed (LB), still water (SW), or straight flow (SF). The second part indicates the water depth (cm). The third part is an index pertaining to the mean flow velocity for straight flow experiments. The second part in the live-bed experiment indicates that a bubble screen was applied.
[b]Blanckaert et al. (2008) experiment.

04014070-4

Blanckaert et al. (2008), the value $\psi = -1\,10^{-3}$ m^2 s^{-1} was adopted as a criterion to delimit the size of the bubble-induced secondary flow.

Results

Effects of Flow Shallowness and Base Flow Velocity on the Bubble-Induced Secondary Flow

These experiments aimed at analyzing the effects of the flow shallowness and the base flow velocity on the strength and size of the bubble-induced secondary flow. Furthermore, they aimed at providing reference data for comparison with the mobile-bed experiment. Experiments were conducted under both still-water and straight-flow conditions with three different water depths, as follows: (1) $H = 0.11$ m, (2) $H = 0.16$ m, and (3) $H = 0.21$ m (Table 2). For each water depth, experiments were performed with four different base flow velocities **U**, as follows: (1) **U** $= 0$ m s^{-1} (still-water condition), (2) **U** $= 0.09$–0.10 m s^{-1}, (3) **U** $= 0.19$ m s^{-1}, and (4) **U** $= 0.28$–0.29 m s^{-1} (Table 2). For $H = 0.16$ m, the Blanckaert et al. (2008) experiment in the same flume with **U** $= 0.43$ m s^{-1} is also included in the analysis. Fig. 3 illustrates the bubble-induced secondary flow by means of the streamfunction ψ and the vector patterns of secondary flow ($\mathbf{v_y}$, $\mathbf{v_z}$) for experiments performed with the same base flow velocity **U** $= 0.28$ m s^{-1} at three different water depths.

The measured patterns show that the water depth controls the size and strength of the bubble-induced secondary flow, which increase with higher water depths. The bubble-induced secondary flow covers the region $y = 0.13$–0.45 m ($\sim 3.0H$), for $H = 0.11$ m [Fig. 3(a)]; the region $y = -0.06$ to 0.45 m ($\sim 3.2H$), for $H = 0.16$ m [Fig. 3(b)]; and it extends from $y = -0.25$ to 0.45 m ($\sim 3.4H$), for $H = 0.21$ m [Fig. 3(c)].

These results are in line with previous studies performed under still-water conditions (Wen and Torrest 1987; Fanneløp et al. 1991;

Riess and Fanneløp 1998) where the bubble-induced secondary flow size was proportional to the water depth and had a size of $2.5H$ to $7H$.

The strength of the bubble-induced secondary flow can be parameterized by means of the maximum value attained by the streamfunction ψ_m. Based on the Blanckaert et al. (2008) experiment, ψ_m is observed at a distance of about H from the bubble screen, which would correspond to $y = 0.34$, 0.29, and 0.25 m in the experiments with a flow depth of $H = 0.11$, 0.16, and 0.21 m, respectively. These locations are near the edge of the measuring grid. The patterns (Fig. 3) confirm that ψ_m is situated outside the measuring grid in the experiments with $H = 0.11$ m. Hence the maximum measured value of $\psi = -4.1\,10^{-3}$ m^2 s^{-1} [Fig. 3(a)] underestimates the real ψ_m. The patterns for the experiments with $H = 0.16$ and 0.21 m suggest that the maximum measured values of $\psi = -6.7\,10^{-3}$ m^2 s^{-1} [Fig. 3(b)] and $\psi = -8.8\,10^{-3}$ m^2 s^{-2} [Fig. 3(c)], respectively, are good approximations of ψ_m. These results indicate the strength of the bubble-induced secondary flow increases with the water depth.

Similar streamfunction patterns were obtained for all 13 experiments covering three flow depths, and five base flow conditions (Table 2) and the main results of all cases are summarized (Fig. 4). For each of the investigated water depths the secondary flow patterns are about identical for the five investigated base flow velocities, and the size of the bubble-induced secondary flow cell is not significantly influenced by the base flow velocity, and is consistently about 3.4 ± 0.7 the water depth [Fig. 4(a)]. This means that the base flow parallel to the bubble screen is mainly advecting the bubble-induced secondary flow pattern in downstream direction without significantly modifying it. The increase of ψ with increasing water depth (Fig. 3) was to be expected because the definition of ψ includes integration with respect to the water depth [Eqs. (3)–(5)]. The depth-scaled streamfunction ψ/H provides a measure for the magnitude of the secondary flow vectors ($\mathbf{v_y}$, $\mathbf{v_z}$) in the bubble-induced secondary flow cell. Fig. 4(b) shows that ψ_m/H is in all 13 experiments within the range
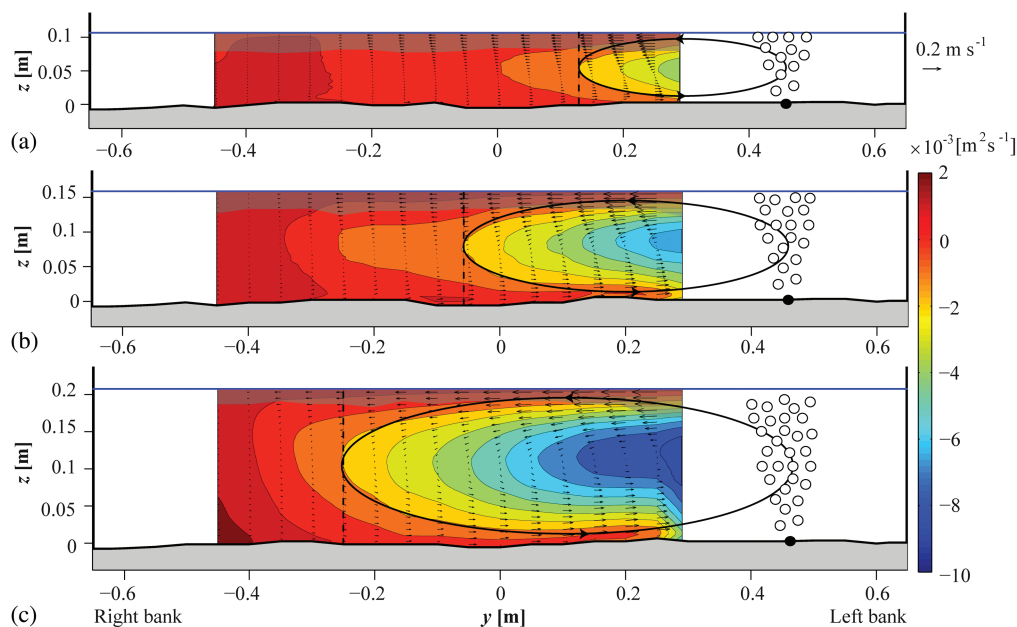
Fig. 3. (Color) Cross-sectional patterns of bubble-induced secondary flow in the straight-flow experiments (Table 2): (a) SF_11_3; (b) SF_16_3; (c) SF_21_3; streamfunction $\psi 10^3$ (m^2 s^{-1}, color isolines) and bubble-induced secondary flow ($\mathbf{v_y}$, $\mathbf{v_z}$), vector representation; the shaded area near the water surface indicates extrapolated values; the dashed lines indicate the value $\psi = -1\,10^{-3}$ m^2 s^{-1} which is chosen as criterion to delimit the secondary flow cell
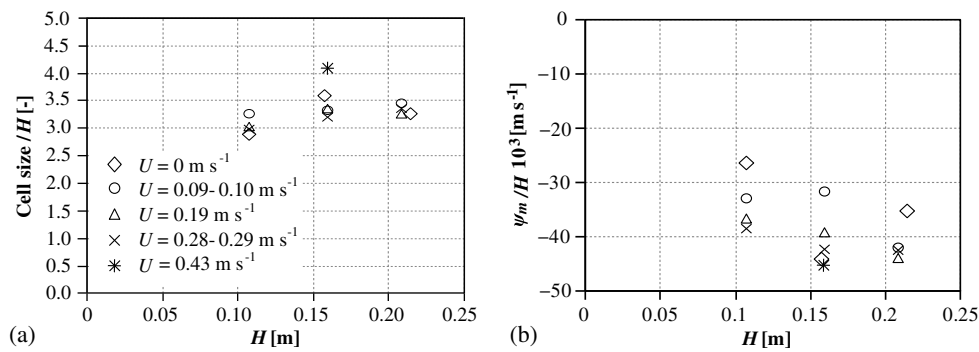
Fig. 4. Dependence of characteristics of the bubble-induced secondary flow on the water depth H for the five different base flow velocity conditions: (a) normalized size; (b) depth-scaled maximal intensity ψ_m/H

-0.035 ± 0.010 m s^{-1}. As previously mentioned, the maximum measured values of ψ underestimate the real value of ψ_m for the experiments with a water depth of $H = 0.11$ m because ψ_m occurs outside the measuring grid. Therefore, it can be concluded from Fig. 4(b) that the strength of the bubble-induced secondary flow does not significantly depend on the water depth.

Interplay between the Patterns of Longitudinal Flow and the Bubble-Induced Secondary Flow

The bubble-induced secondary flow advects momentum and thereby causes a redistribution of the pattern of longitudinal velocities. Fig. 5 shows the patterns of the normalized longitudinal velocity $\mathbf{v_x}/U$ and the vector pattern of secondary flow $(\mathbf{v_y}, \mathbf{v_z})$ at three different water depths with a base flow of $\mathbf{U} = 0.28$ m s^{-1}. The corresponding patterns of the secondary flow streamfunctions are shown (Fig. 3).

In all experiments, upwards velocities induced by the bubble screen are advecting low momentum fluid originating from the near-bottom zone towards the water surface. The high momentum fluid originating from near the water surface is advected by the bubble-induced secondary flow away from the bubble screen near the water surface leading to a core of maximum longitudinal velocities near the water surface at the outer edge of the bubble-induced secondary flow cell.

Advection by the secondary flow velocities extends the core of highest velocities towards the bubble screen at some distance under the water surface. Due to the combined effect of advection by secondary flow and bottom friction, the core of highest velocities is not found in the lower part of the water column but at about middepth.

The streamfunction measurements (Fig. 4) have shown that the base flow velocity has no significant effect on the characteristics of the bubble-induced secondary flow. It can be expected, however, that the advective redistribution of the longitudinal velocities by the
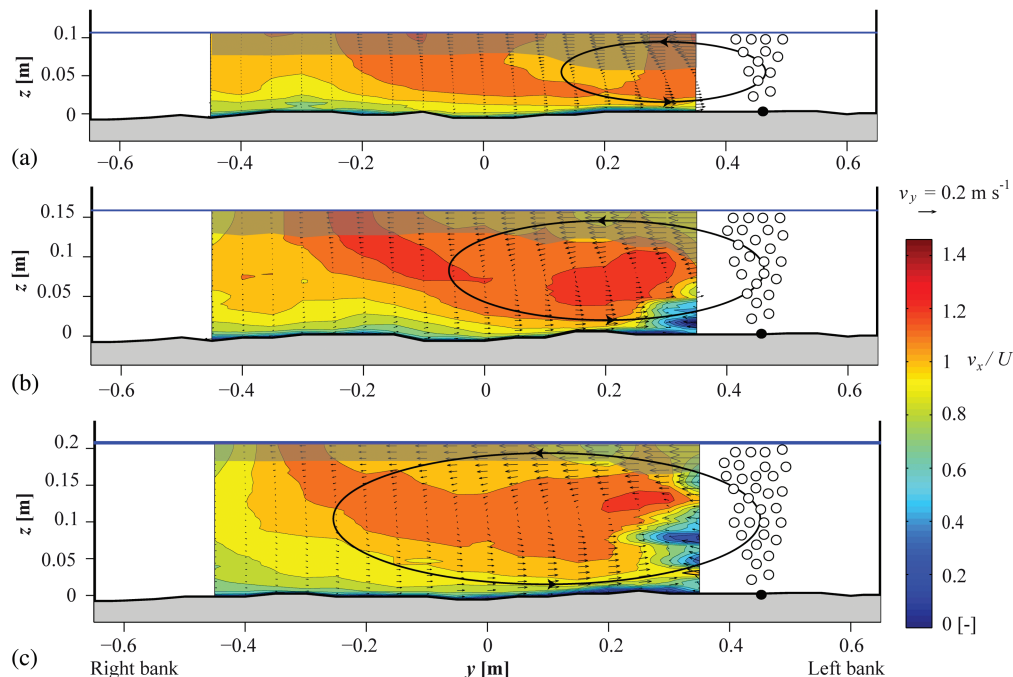
Fig. 5. (Color) Influence of the bubble-induced secondary flow $(\mathbf{v_y}, \mathbf{v_z}$; vector representation), on the normalized longitudinal velocity $\mathbf{v_x}/U$ (color isolines) in the straight-flow experiments (Table 2): (a) SF_11_3; (b) SF_16_3; (c) SF_21_3; the shaded area near the water surface indicates extrapolated values
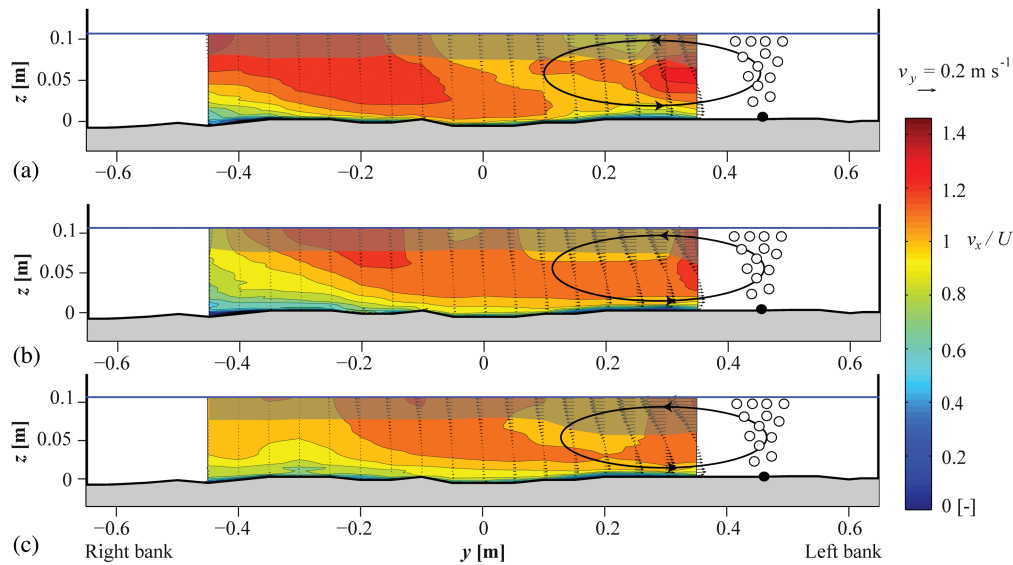
Fig. 6. (Color) Influence of the bubble-induced secondary flow (v_y, v_z; vector representation), on the normalized longitudinal velocity v_x/U (color isolines) in the straight-flow experiments (Table 2): (a) SF_11_1; (b) SF_11_2; (c) SF_11_3; the shaded area near the water surface indicates extrapolated values

secondary flow depends on the base flow velocity. Fig. 6 indicates qualitatively similar patterns for the three investigated base flows in the experiments with water depth of $H = 0.11$ m. Quantitatively, however, the resulting velocity gradients seem to be attenuated with increasing base flow. This can tentatively be attributed to an increase of the diffusive character of the flow with increasing base flow velocity.

Interaction of the Bubble-Screen Induced Flow Structures with the Bed Morphology, the Base Flow, and the Sediment Transport

The bubble-induced secondary flow redistributes the velocities, and can therefore be expected to redistribute the sediment transport and modify the resulting bed morphology under mobile-bed conditions. Fig. 7 illustrates the equilibrium morphology in the mobile-bed LB_B experiment with bubble screen. The final channel-averaged bed level defines the reference level ($z = 0$ m). In the initial zone ($x = 1$ m to about $x = 2.5$ m), two scour holes form at each side of the bubble screen, as follows: (1) situated at the toe of the bank adjacent to the bubble screen, and (2) located about 0.3-m away from the bubble screen. From about $x = 2.5$ m onward, the right

scour hole widens in downstream direction and moves away from the bubble screen, and it attains the right bank at the channel exit. Sediment scoured in both scour holes is transported towards the bubble screen by the bubble-induced secondary flow and leads to the development of a deposition bar centered on the porous tube.

This morphological development suggests that an interaction exists between the bubble-induced secondary flow, the base flow, and the morphology, which seems to lead to a strengthening of the processes. Moreover, it suggests that a longer longitudinal distance is required under mobile-bed conditions than under immobile-bed conditions to attain equilibrium between the base flow, the bubble-induced secondary flow, and the morphology.

In order to explain the influence of the bubble-induced secondary flow on the equilibrium morphology in the initial part of the channel, the streamfunction patterns measured in the SF_16_2 and LB_B experiments are drawn in the same cross section at $x = 3$ m [Figs. 8(a and b)], respectively. In addition, Fig. 8(c) shows the pattern of longitudinal velocities and the vector pattern of the secondary flow (v_y, v_z) in the LB_B experiment in the same cross section. The sizes of the secondary flow in the SF_16_2 and LB_B experiments are similar, which indicates that the immobile-bed experiment may be representative for the initial conditions in the
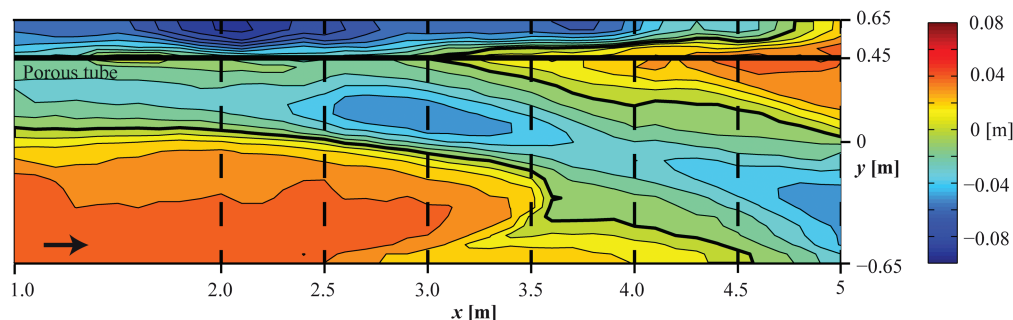
Fig. 7. (Color) Isolines of the equilibrium bed level with an interval of 0.01 m derived from laser distometer measurements for the LB_B experiment; the bold line represents the $z = 0$ m contour and delimits scour and deposition zones; the dashed lines indicate cross sections where velocity measurements have been performed
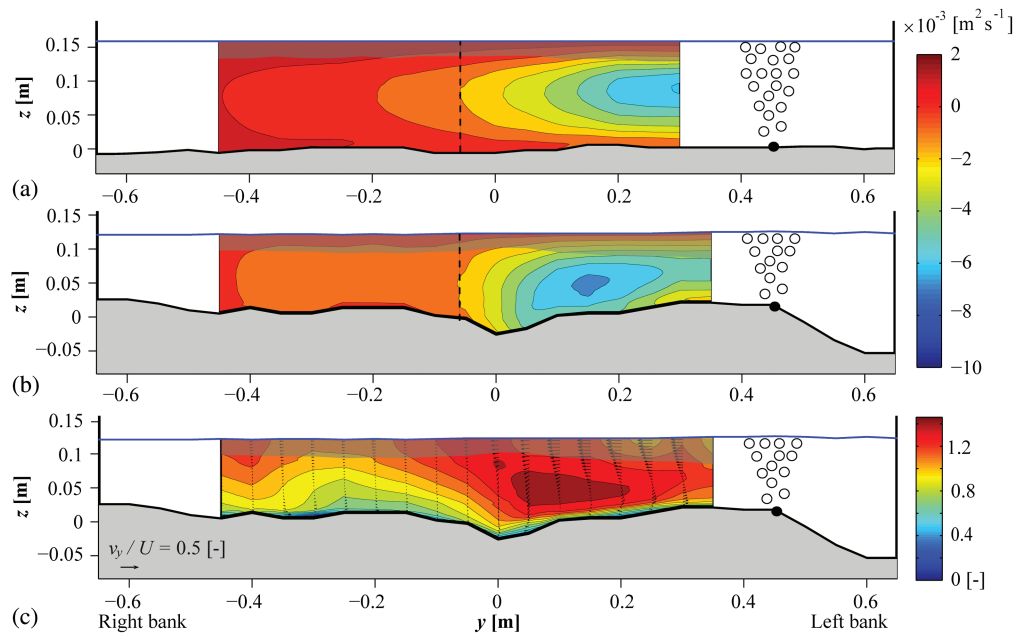
Fig. 8. (Color) Bubble-induced secondary flow in the cross section at $x = 3$ m: (a) straight-flow experiment SF_16_2; (b) mobile-bed experiment LB_B, streamfunction $\psi 10^{-3}$ (m² s⁻¹); the dashed lines indicate the value $\psi = -1 \, 10^3$ m² s⁻¹ which is chosen as criterion to delimit the secondary flow cell; (c) mean normalized longitudinal velocities $\mathbf{v_x}$ (contours) and cross-sectional velocities ($\mathbf{v_y}$, $\mathbf{v_z}$; vectors) in the same cross section for the LB_B experiment; the shaded area near the water surface indicates extrapolated values

mobile-bed experiment when the morphological adjustment starts. Vertical downward velocities are about zero in the core of the bubble-induced secondary flow cell and increase to their maximum value near the outer edge of the cell, where they impinge on the bed. As explained previously, advective momentum transport by the secondary flow redistributes the longitudinal velocity and causes the core of maximum longitudinal velocities to be situated in the lower part of the water column in region covered by the outer half of the secondary flow cell. This enhances the bed shear stress and the turbulence, and the sediment transport capacity. The vertical velocities impinging on the bed, and the redistribution of the longitudinal velocities, explain the development of bed scour in the region covered by the outer half of the secondary flow cell. The transverse component of the secondary flow is directed away from the bubble screen over the entire flow depth. This transverse component can be decomposed into two contributions, as follows: (1) with zero depth-averaged value that represents a secondary flow cell, and (2) constant over the flow depth and represents a bulk transverse transport of mass. The latter is outward directed, which concurs with the outwards shift of the scour hole farther downstream (Fig. 7).

Fig. 9 shows the patterns of the normalized longitudinal velocity and the bubble-induced secondary flow measured in three different cross sections at (1) $x = 2.5$-m, (2) 3.5-m, and (3) 4.5-m downstream from the beginning of the bubble screen. In each cross section, scour occurs in the region covered by the outer half of the bubble-induced secondary flow cell and the maximum scour occurs near the outer edge of the cell where vertical velocities impinge on the bed. In the three cross sections, the transverse component of the secondary flow is directed away from the bubble screen over the entire flow depth, which concurs with the outwards shift of the scour hole farther downstream (Fig. 7). At $x = 2.5$ m, the maximal scour is at $y = 0.15$ m [Fig. 9(a)], whereas it extends from $y = 0$ to 0.2 m at $x = 3.5$ m [Fig. 9(b)] to finally covers half of the cross section from $y = -0.4$ to 0.15 m at $x = 4.5$ m [Fig. 9(c)].

These results show a strengthening of processes. Scour extent as well as the bubble-induced secondary flow size widen with increasing x. Fig. 10(a) summarizes the growth of the size and the strength of the bubble-induced secondary flow cell, both normalized with the flume-averaged flow depth. The secondary flow cell grows about linearly in longitudinal direction [Fig. 10(a)] and almost reaches the right bank at the flume exit, where its size reached a maximum value of about $6.5H$. At $x = 3.5$ m, topographic steering by a dune front in the right half of the cross section causes some additional flow redistribution away from the bubble screen that contributes to the widening of the cell and explains the maximum value of the cell size recorded in that cross section. The strength of the bubble-induced secondary flow does not show a clear longitudinal evolution, and is characterized by values in the range $\psi_m/H = -0.075 \pm 0.025$ m s⁻¹. This is about 2× the strength that was observed in the immobile-bed experiments. This implies that the bubble-induced secondary flow cell mainly grows in longitudinal direction, but that the secondary flow velocities involved do not reveal any trend.

Discussion

Interaction between the Air-Bubble Screen, the Bubble-Induced Secondary Flow, and the Morphology

The experimental observations indicate a mutually strengthening interaction between the air-bubble screen, the bubble-induced secondary flow, and the morphology.

A first mutually strengthening interplay exists between the rising air bubbles and the bubble-induced secondary flow cell. According to Leifer et al. (2000), the rising velocity of a single air bubble is approximately constant at $\mathbf{v}_{z,bubble,0} = 0.24$ m s⁻¹ in the range of applied bubble sizes, independent of the flow depth. A bubble screen, however, entrains surrounding water and induces a secondary flow cell with maximum vertical flow velocities $\mathbf{v}_{z,flow}$

© ASCE

J. Hydraul. Eng.
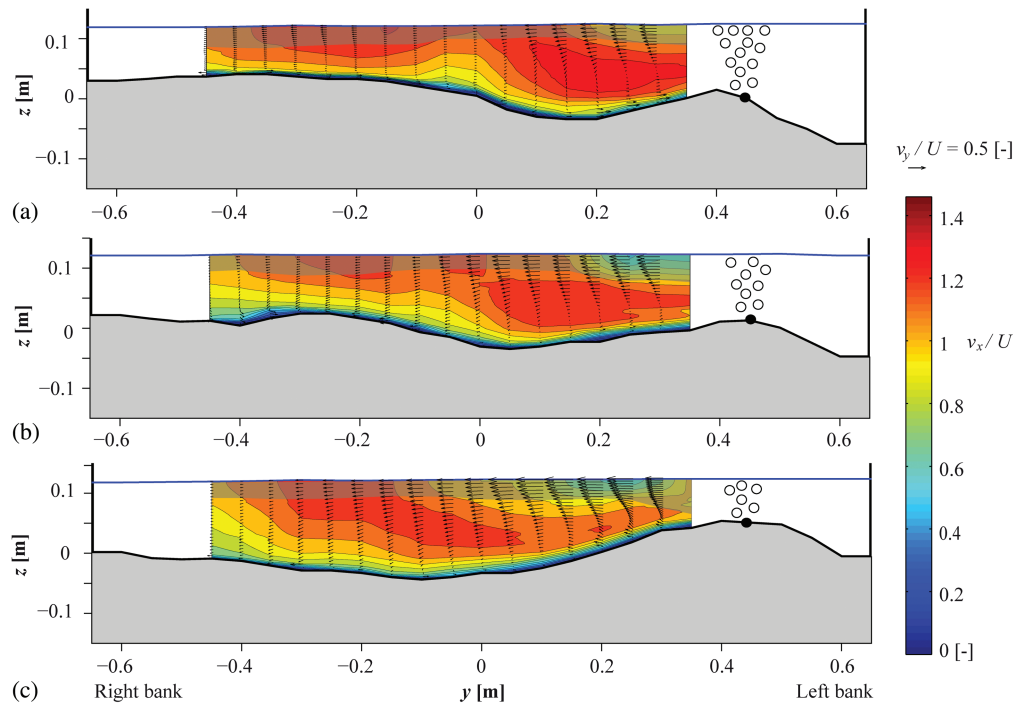
Fig. 9. (Color) Mean normalized longitudinal velocities $\mathbf{v_x}$ (contours) and cross-sectional velocities ($\mathbf{v_y}$, $\mathbf{v_z}$: vectors), at three measured cross sections in LB_B experiment; the shaded areas near the water surface indicate extrapolated values
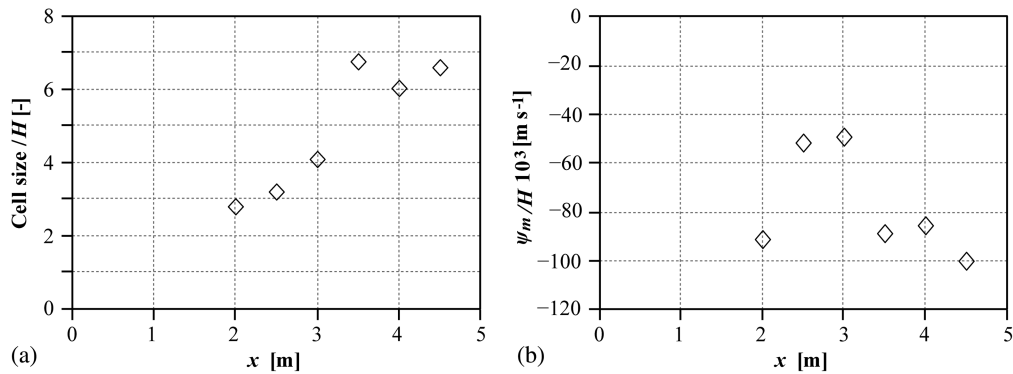
Fig. 10. Longitudinal evolution of the bubble-induced secondary flow characteristics in the LB_B mobile-bed experiment: (a) normalized cell size; (b) depth-averaged maximal intensity ψ_m/H (to be compared to Fig. 4 for the immobile-bed experiments)

situated in the vertical profile above the porous tube. These vertical flow velocities advect the rising air-bubbles and thereby increase the rising velocity of the air-bubbles to

$$\mathbf{v_{z,bubble}} = \mathbf{v_{z,bubble,0}} + \mathbf{v_{z,flow}} \tag{6}$$

This increased rising speed can be expected to increase the quantity and the velocity of water entrained by the rising air-bubbles, and hence to amplify the secondary flow cell. In first approximation, this mutually strengthening interaction can be quantified by expressing the efficiency η of the rising air bubbles to entrain water as

$$\eta = \frac{\mathbf{v_{z,flow}}}{\mathbf{v_{z,bubble}}} = \frac{\mathbf{v_{z,flow}}}{\mathbf{v_{z,bubble,0}} + \mathbf{v_{z,flow}}} = 1 - \frac{\mathbf{v_{z,bubble,0}}}{\mathbf{v_{z,bubble,0}} + \mathbf{v_{z,flow}}} \tag{7}$$

Eqs. (6) and (7) straightforwardly lead to

$$\mathbf{v_{z,bubble}} = \frac{\mathbf{v_{z,bubble,0}}}{1 - \eta} \tag{8}$$

Although no velocity measurements could be made in the region covered by the air-bubble screen, the final rising velocity of the air bubbles, $\mathbf{v_{z,bubble}}$, and the water entrainment efficiency, η, can be estimated from the measured patterns of the transverse velocity $\mathbf{v_y}$ as described next. According to Wen and Torrest (1987), the vertical flow velocities above the porous tube are zero at the bed and the water surface, and reach a maximum value, $\mathbf{v_{z,flow,max}}$, at about middepth (Fig. 11). Assuming then a parabolic velocity distribution over the depth, the depth-averaged vertical velocity $\mathbf{v_{z,flow}}$ equals two-thirds of the maximum vertical velocity, $\mathbf{v_{z,flow,max}}$. Mass conservation in the secondary flow cell relates $\mathbf{v_{z,flow,max}}$ to the maximum transverse velocity near the water surface directed away from
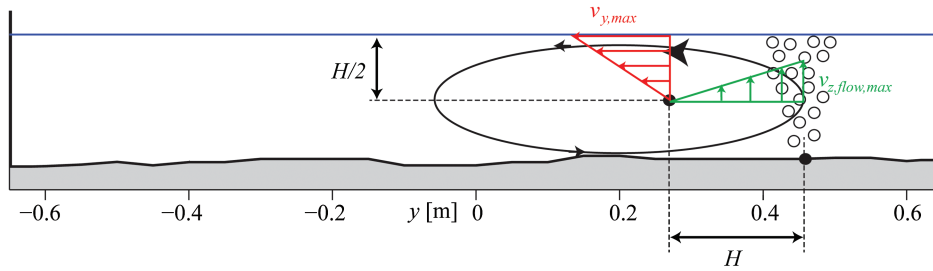
Fig. 11. (Color) Schematical representation of the asymmetrical bubble-induced secondary flow cell and the application of the principle of mass conservation to the secondary flow cell

the bubble screen, $v_{y,max}$, which occurs at a distance of about $1H$ away from the bubble screen (Figs. 5, 6, 8, 9), as schematically represented (Fig. 11)
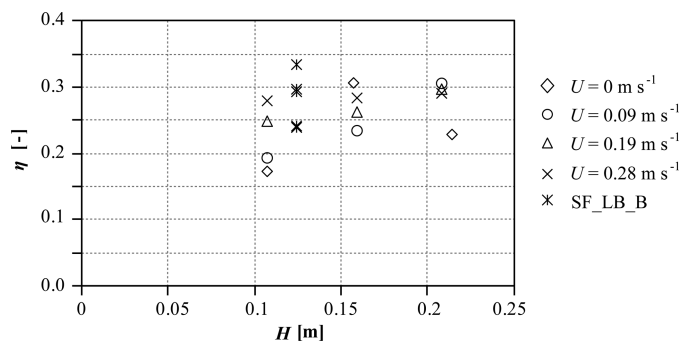
$$v_{y,max}\frac{H}{2} = v_{z,flow,max}H = \frac{3}{2}v_{z,flow}H \quad \text{or} \quad v_{z,flow} = \frac{1}{3}v_{y,max} \tag{9}$$

leading to

$$v_{z,bubble} = v_{z,bubble,0} + \frac{1}{3}v_{y,max} \tag{10}$$

$$\eta = 1 - \frac{v_{z,bubble,0}}{v_{z,bubble,0} + (\frac{1}{3})v_{y,max}} \tag{11}$$

Based on the measured patterns of the transverse velocity v_y (Figs. 5, 6, 8, 9), both quantities have been estimated in the range $v_{z,bubble} = 0.33 \pm 0.04$ m s^{-1}, and $\eta = 0.25 \pm 0.08$ for all experiments (Fig. 12). This means that the vertical velocity of the entrained water was about 25% of the rising velocity of the air bubbles, which defines the water entrainment efficiency. According to Eq. (8), this means that the mutually strengthening interaction between the rising air bubbles and the bubble-induced secondary flow cell increased the rising speed of the bubbles by about 33% as compared to the rising speed of an individual air-bubble that would not induce secondary flow. The water depth and the base flow velocity did not considerably influence the water entrainment efficiency in the range of investigated depths. As expected, the water entrainment efficiency of the air bubbles was similar in the immobile-bed and mobile-bed experiments. The water entrainment efficiency can, however, be expected to depend on the air discharge, which was identical in all reported experiments. This is, as far as

the writers know, the first quantitative estimation of how efficient are the rising air-bubbles in entraining water.

A second mutually strengthening interplay exists between the bubble-induced secondary flow cell and the morphological redistribution. The morphological redistribution increases the flow depth in the region covered by the secondary flow cell, which increases the size and strength of the latter, because both were found to scale with the flow depth. This in turn enhances the redistribution of the velocity and the bed shear stress, and hence the morphological redistribution. The larger depth-averaged size and strength of the bubble-induced secondary flow cell in the mobile-bed configuration than in the immobile-bed configuration further confirms and illustrates this mutually strengthening interaction, which is favorable for the application of the bubble-screen technique with morphodynamic purposes in shallow rivers and open channels.

Relevance for Application in Natural Rivers and Open Channels

The reported experimental results demonstrate that the bubble screen can modify the flow patterns and the bed morphology in shallow laboratory open channels under conditions of live-bed sediment transport and subcritical flow. Hereafter, some further issues are discussed that are relevant to applications of the bubble screen technique in shallow rivers or open channels.

The reported experiments performed in a shallow laboratory flume with a maximal investigated water depth $H = 0.21$ m resulted in secondary flow cells with a size of $3\times$ (immobile bed) to $7\times$ (mobile bed) the flow depth, independent of the base flow velocity and flow depth. Experiments performed under still-water conditions reported in literature (Table 1) have shown that the bubble-induced secondary flow size varies from 2.5 to $7\times$ the water depth, independent of the water depth (Riess and Fanneløp 1998), whereby differences between results are mostly related to the different definitions of the bubble-induced secondary flow size or to the different geometries of experimental setups. Wen and Torrest (1987), for example, found a secondary flow cell size of $4H$ for water depths between 0.25 and 0.9 m. Goossens (1979) performed experiments at small and large scales and found a range of influence of about $4\times$ the water depth, for water depths between 2 and 5 m. These results indicate that similar secondary flow cell sizes (normalized with the water depth) are found independently of the water depth and base flow velocity, and that the results obtained in the here reported laboratory experiments are relevant for natural rivers and open channels with subcritical flow conditions.

For the range of bubble sizes used, the rising velocity of an individual air bubble in water is nearly constant at 0.24 m s^{-1} (Leifer et al. 2000), irrespective of the flow depth. This implies that the bubble-induced secondary flow velocities will be of similar magnitude in a laboratory flume and a natural river. The previous

Fig. 12. Dependence of the water entrainment efficiency η on the flow depth H for all investigated experimental conditions

experiments (Blanckaert et al. 2008; Dugué et al. 2013) and the research reported in this paper indicate secondary flow velocities of approximately 0.2 m s^{-1}.

The efficiency of bubble-induced secondary flow velocities, of approximately 0.2 m s^{-1}, to redistribute velocities, boundary shear stresses, and morphology will depend on numerous factors including the type of application (bend scour, bridge pier scour, and so on), the geometrical configuration, flow conditions, and sediment characteristics. As previously mentioned, in most applications the bubble-screen technique is based on the principle that the rising air bubbles counteract downward vertical velocities impinging on the riverbed, such as found near the outer bank in open-channel bends or on the upstream-looking face of bridge piers. The efficiency will therefore mainly depend on the magnitude of these downward vertical velocities impinging on the riverbed. Chapter 7 of Dugué (2013) made a detailed analysis of the application range of the bubble-screen technique to counteract scour in open-channel bends.

A larger river will require a larger air discharge in order to induce the secondary flow velocities of the order of 0.2 m s^{-1}. Brevik (1977) has proposed a semitheoretical model that relates the maximum transverse velocity at the water surface induced by the bubble screen, $\mathbf{v_{y,max}}$, to the air discharge Q_a required

$$Q_a = \left(\frac{\mathbf{v_{y,\,max}}}{1.7}\right)^3 \frac{1}{g}\left(1 + \frac{H}{H_a}\right)L \qquad (12)$$

where H_a = atmospheric pressure head (m), expressed as the equivalent of 10-m high water column. Blanckaert et al. (2008) and Chapter 7 of Dugué (2013) estimated the operational cost of applying a bubble screen in natural open-channel bends and compared the required air discharge to other typical applications of bubble screens, such as lake destratification and oxygen suppletion in ice-covered rivers. Their results suggest that the bubble-screen technique is economically feasible.

The application of bubble screens typically involves highly turbulent flows, where the Reynolds number is an important scaling parameter. Koken et al. (2013) have shown that turbulence structures and characteristics in open-channel bends are very similar in laboratory flumes and natural rivers, in spite of the considerably differences in Reynolds number. Therefore, Reynolds number effects are not expected to be a primary concern in investigations on the applicability of the bubble screen technique.

If the rising air-bubbles are able to overcome the vertical velocities impinging on the river bed in the regions of maximum scour, the bubble screen will be able to redistribute the flow, boundary shear stress, and sediment transport. In most cases, higher base flow velocities will induce stronger vertical velocities impinging on the riverbed and hence reduce the potential efficiency of the bubble-screen technique. Higher base flow velocities typically also lead to coarser riverbed sediment, indicating a decrease of the bubble-screen technique efficiency with increasing sediment size. There is no direct quantitative relation, however, between the size of the riverbed sediment, and the efficiency or application range of the bubble screen.

Typical natural rivers at bankful flow have a width-to-depth ratio of the order of 20 (Blanckaert 2011). With a size of 3–7× the flow depth, the bubble-induced secondary flow is not constrained by the channel width but can induce morphological changes in a substantial part of the channel cross section.

In the mobile bed experiment LB_B (Fig. 7), considerable scour occurred between the bubble screen and the adjacent bank. More research is required to investigate the flow field and its interaction with the morphology in this region, and possibly to optimize the position of the bubble screen relative to the bank. Countermeasures may be required to avoid local scour induced by the air-bubble screen. With the present state of knowledge, the application range of bubble screens should be limited to channels and rivers with fixed protected banks.

The bubble screen technique has already shown promising results for an application in open-channel bends (Blanckaert et al. 2008; Dugué et al. 2013). However, the ability of the bubble screen to redistribute the bed morphology suggests that this technique has an application potential in a variety of configurations. For example, it could be used at the toe of bridge piers of abutments in order to counteract downwards velocities impinging on the bed and shift the location of maximum scour away from the structure. A fixed layer may be required in the narrow region between the bubble screen and the structure to avoid scour. A bubble screen could also be applied to avoid deposition in a determined zone of the riverbed or to create preferential corridors for sediment transport. As an example, they could be used to prevent silting in harbors by guiding the mean longitudinal velocities and consequently the sediment-laden flows.

Conclusion

In the reported shallow-flow laboratory experiments, rising air bubbles generated by a pressurized porous tube situated on the bed entrained the surrounding water and induced secondary flow perpendicular to the porous tube. In the investigated range of conditions, based on both theoretical considerations and experimental results, the vertical velocity of the entrained water was estimated to be about 25% of the rising velocity of the air bubbles, which defines the water entrainment efficiency. The bubble-induced secondary flow redistributed the pattern of the longitudinal velocity, which caused morphological redistribution under mobile-bed conditions.

The strength and size of the bubble-induced secondary flow were independent of the base flow velocity, which mainly advected the bubble-induced secondary flow downstream without modifying its characteristics. The size of the bubble-induced secondary flow cell ranged from 3× (immobile bed) to 7× (mobile bed) the water depth, and also the strength primarily scaled with the water depth. Similar sizes of bubble-induced secondary flow cells have been reported in literature for water depths ranging from 0.1 to 5 m. This indicates that the processes are not primarily scale dependent, and that the findings of the laboratory investigation are therefore relevant for natural rivers and open channels.

A mutually strengthening interplay occurred between the bubble screen, the bubble-induced secondary flow, and the morphology. Advection by the bubble-induced secondary flow considerably increased the rising velocity of the air bubbles (as compared to the rising velocity of a single air bubble in still water) and hence also the rising velocity of the entrained water, which on its turn strengthened the bubble-induced secondary flow. The morphological redistribution increased the flow depth in the region covered by the bubble-induced secondary flow, which caused an increase in size and strength of the secondary flow cell. This in turn, enhanced the morphological redistribution. When scaled with the water depth, the size and strength of the bubble-induced secondary flow cell were larger in the mobile-bed configuration than in the immobile-bed configuration, which confirms and illustrates this mutually strengthening interplay.

The results show the potential of the bubble-screen technique to modify the morphology in a variety of applications in shallow rivers and open channels.

Acknowledgments

Notation

The following symbols are used in this paper:

A = buoyancy of the bubble screen (m s^{-1});

B = channel width (m);

b = distance between the air-line source and the opposite bank (m);

d_m = mean sediment size diameter (m);

g = gravitational acceleration (m s^{-2});

Fr = water flow Froude number (dimensionless);

H = cross-sectional averaged water depth (m);

H_a = atmospheric pressure head (m);

L = length of the air-line source (m);

Q = water discharge ($\text{m}^3\,\text{s}^{-1}$);

Q_a = air discharge ($\text{m}^3\,\text{s}^{-1}$);

q_a = air discharge per unit of air-line source length ($\text{m}^3\,\text{s}^{-1}\,\text{m}^{-1}$);

q_f = water discharge per unit width ($\text{m}^3\,\text{s}^{-1}\,\text{m}^{-1}$);

q_s = sediment discharge per unit width ($\text{kg}\,\text{m}^{-1}\,\text{s}^{-1}$);

R = inertial force of the river flow (m s^{-1});

$\mathbf{U}$ = cross-sectional averaged mean velocity (m s^{-1});

$\mathbf{v_i}(i = x, y, z)$ = time-averaged velocity component along i-direction (m s^{-1});

$\mathbf{v_{y,max}}$ = maximal transversal velocity induced by the bubble screen (m s^{-1});

$\mathbf{v_{z,bubble}}$ = final rising velocity of the air bubbles in the bubble screen (m s^{-1});

$\mathbf{v_{z,bubble,0}}$ = final rising velocity of a single air bubble (m s^{-1});

$\mathbf{v_{z,flow}}$ = vertical flow velocity observed in the bubble screen (m s^{-1});

$\mathbf{v_{z,flow,max}}$ = maximal upward velocity observed in the bubble screen (m s^{-1});

x, y, z = longitudinal, transversal, and vertical reference axis;

y_{max}, y_{min} = transverse limit of the ADVP measurements (m);

z_b = bed level (m);

η = water entrainment efficiency (dimensionless);

ψ = streamfunction defined according to Eq. (3) ($\text{m}^2\,\text{s}^{-1}$);

ψ_m = maximal intensity of the streamfunction ($\text{m}^2\,\text{s}^{-1}$);

ψ_y = transversal streamfunctions ($\text{m}^2\,\text{s}^{-1}$); and

ψ_z = vertical streamfunction ($\text{m}^2\,\text{s}^{-1}$).

References

Batchelor, G. K. (1967). *An introduction to fluid dynamics*, Cambridge University Press, Cambridge, U.K.

Blanckaert, K. (2010). "Topographic steering, flow recirculation, velocity redistribution, and bed topography in sharp meander bends." *Water Resour. Res.*, 46, W09506.

Blanckaert, K. (2011). "Hydrodynamic processes in sharp meander bends and their morphological implications." *J. Geophys. Res.*, 116, F01003.

Blanckaert, K., Buschman, F. A., Schielen, R., and Wijbenga, J. H. A. (2008). "Redistribution of velocity and bed-shear stress in straight and curved open-channels by means of a bubble screen: Laboratory experiments." *J. Hydraul. Eng.*, 10.1061/(ASCE)0733-9429(2008)134:2(184), 184–195.

Blanckaert, K., and Graf, W. H. (2004). "Momentum transport in sharp open-channel bends." *J. Hydraul. Eng.*, 10.1061/(ASCE)0733-9429(2004)130:3(186), 186–198.

Blanckaert, K., and Lemmin, U. (2006). "Means of noise reduction in acoustic turbulence measurements." *J. Hydraul. Res.*, 44(1), 3–17.

Bombardelli, F. A., Buscaglia, G. C., Rehmann, C. R., Rincón, L. E., and García, M. H. (2007). "Modelling and scaling of aeration bubble plumes: A two-phase flow analysis." *J. Hydraul. Res.*, 45(5), 617–630.

Brevik, I. (1977). "Two-dimensional air-bubble plume." *J. Waterw. Port Coastal Ocean Div.*, 103(1), 101–115.

DeMoyer, C. D., Schierholz, E. L., Gulliver, J. S., and Wilhelms, S. C. (2003). "Impact of bubble and free surface oxygen transfer on diffused aeration systems." *Water Res.*, 37(8), 1890–1904.

Dugué, V. (2013). "Influencing river morphodynamics by means of a bubble screen: Application to open-channel bends." Ph.D. thesis, Ecole Polytechnique Fédérale de Lausanne, Lausanne, Switzerland.

Dugué, V., Blanckaert, K., Chen, Q., and Schleiss, A. J. (2013). "Reduction of bend scour with an air-bubble screen—Morphology and flow patterns." *Int. J. Sediment Res.*, 28(1), 15–23.

FannELøp, T. K., Hirschberg, S., and Küffer, J. (1991). "Surface current and recirculating cells generated by bubble curtains and jets." *J. Fluid Mech.*, 229(1), 629–657.

García, C. M., and García, M. H. (2006). "Characterization of flow turbulence in large-scale bubble-plume experiments." *Exp. Fluids*, 41(1), 91–101.

Goossens, L. (1979). "Reservoir destratification with bubble columns." Ph.D. thesis, Delft Univ., Delft, Netherlands.

Hurther, D., and Lemmin, U. (1998). "A constant-beam-width transducer for 3D acoustic Doppler profile measurements in open-channel flows." *Meas. Sci. Technol.*, 9(10), 1706–1714.

Koken, M., Constantinescu, G., and Blanckaert, K. (2013). "Hydrodynamic processes, sediment erosion mechanisms, and Reynolds-number-induced scale effects in an open channel bend of strong curvature with flat bathymetry." *J. Geophys. Res. Earth Surf.*, 118(4), 2308–2324.

Leifer, I., Patro, R. K., and Bowyer, P. (2000). "A study on the temperature variation of rise velocity for large clean bubbles." *J. Atmos. Ocean Technol.*, 17(10), 1392–1402.

Lemmin, U., and Rolland, T. (1997). "Acoustic velocity profiler for laboratory and field studies." *J. Hydraul. Eng.*, 10.1061/(ASCE)0733-9429(1997)123:12(1089), 1089–1098.

Nakai, M., and Arita, M. (2002). "An experimental study on prevention of saline wedge intrusion by an air curtain in rivers." *J. Hydraul. Res.*, 40(3), 333–339.

Neto, I. E. L., Zhu, D. Z., and Rajaratnam, N. (2008). "Effect of tank size and geometry on the flow induced by circular bubble plumes and water jets." *J. Hydraul. Eng.*, 10.1061/(ASCE)0733-9429(2008)134:6(833), 833–842.

Neto, I. E. L., Zhu, D. Z., Rajaratnam, N., Yu, T., Spafford, M., and McEachern, P. (2007). "Dissolved oxygen downstream of an effluent outfall in an ice-covered river: Natural and artificial aeration." *J. Environ. Eng.*, 10.1061/(ASCE)0733-9372(2007)133:11(1051), 1051–1060.

Rensen, J., and Roig, V. (2001). "Experimental study on the unsteady structure of a confined bubble plume." *Int. J. Multiphase Flow*, 27(8), 1431–1449.

Riess, I. R., and FannELøp, T. K. (1998). "Recirculating flow generated by line-source bubble plumes." *J. Hydraul. Eng.*, 10.1061/(ASCE)0733-9429(1998)124:9(932), 932–940.

Sager, D. R., Hocutt, C. H., and Stauffer, J. R. (1987). "Estuarine fish responses to strobe light, bubble curtains and strobe light bubble-curtain combinations as influenced by water-flow rate and flash frequencies." *Fish. Res.*, 5(4), 383–399.

Sahoo, G. B., and Luketina, D. (2006). "Response of a tropical reservoir to bubbler destratification." *J. Environ. Eng.*, 10.1061/(ASCE)0733-9372 (2006)132:7(736), 736–746.

Schladow, S. G. (1992). "Bubble plume dynamics in a stratified medium and the implications for water quality amelioration in lakes." *Water Resour. Res.*, 28(2), 313–321.

Welton, J. S., Beaumont, W. R. C., and Clarke, R. T. (2002). "The efficacy of air, sound and acoustic bubble screens in deflecting Atlantic salmon, Salmo salar L., smolts in the River Frome, UK." *Fish. Manage. Ecol.*, 9(1), 11–18.

Wen, J., and Torrest, R. S. (1987). "Aeration-induced circulation from line sources. 1. Channel flows." *J. Environ. Eng.*, 10.1061/(ASCE)0733 -9372(1987)113:1(82), 82–98.

Wüest, A., Brooks, N. H., and Imboden, D. M. (1992). "Bubble plume modeling for lake restoration." *Water Resour. Res.*, 28(12), 3235–3250.